Electronic supplementary information

Cyclophane with eclipsed pyrene units enables construction of spin interfaces with chemical accuracy

Marvin Metzelaars,[a] Sebastian Schleicher,[b] Takuma Hattori,[†b] Bogdana Borca,[bc] Frank Matthes,[b] Sergio Sanz,[b] Daniel E. Bürgler,[*b] Jeff Rawson,[‡*ab] Claus M. Schneider[b] and Paul Kögerler[ab]

[a] Institute of Inorganic Chemistry, RWTH Aachen University, 52074 Aachen, Germany.

[b] Peter Grünberg Institute (PGI-6), Forschungszentrum Jülich, 52428 Jülich, Germany.

[c] National Institute of Materials Physics, Atomistilor 405A, Magurele, 077125, Ilfov, Romania.

† present address: Institute for Solid State Physics, The University of Tokyo, Kashiwa, Chiba 277-8581, Japan.

‡ present address: Department of Chemistry and Chemical Biology, Harvard University, Cambridge, MA 02138, USA.

* corresponding authors; Email: d.buergler@fz-juelich.de; jrawson@gmwgroup.harvard.edu
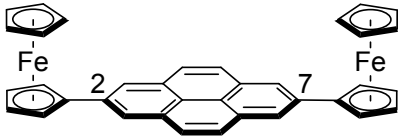
Materials and methods

All commercial chemicals were used as received, except for pyrene (Py) and ferrocene (Fc), which were purified by column chromatography (SiO$_2$, eluent: *n*-hexane) and sublimation, respectively. 1,1'-Bis(di-*tert*-butylphosphino)ferrocene]dichloropalladium(II) (PdCl$_2$(dtbpf)) was purchased from abcr (99%) and stored at –40 °C in an Ar glove box. *N,N*-dimethylformamide (DMF) was dried by vacuum distillation over CaSO$_4$ and was stored over a molecular sieve under Ar. All reactions were carried out under Ar atmosphere using standard Schlenk line and glove box techniques. Work-up was performed under ambient conditions. The starting materials pyrene-2,7-bis(4,4,5,5-tetramethyl-1,3,2-dioxaborolan) ([Bpin]$_2$pyrene),[1] 1,1'-diiodoferrocene[2] and iodoferrocene[2] were synthesized as previously reported. Ultraviolet-visible (UV-Vis) absorption spectra were recorded on a Shimadzu UV-3600 plus spectrophotometer using 10 mm quartz glass cuvettes (QS, Hellma Analytics). Fourier-transform infrared (FT-IR) spectra were measured on a Bruker Vertex 70 spectrometer equipped with a A225 Platinum ATR unit (diamond crystal). Nuclear magnetic resonance (NMR) experiments were performed on a Bruker Avance III HD 600 MHz NMR spectrometer equipped with a CryoProbe Prodigy. The spectra were recorded in toluene-d8 (99.5 atom %, abcr) and referenced to residual solvent peaks. Elemental analysis (C, H, N) was performed on a vario EL cube (elementar) with thermal conductivity detector. Matrix-assisted laser desorption/ionization (MALDI) high-resolution mass spectrometry (HRMS) experiments were performed on a Thermo Scientific MALDI LTQ Orbitrap XL mass spectrometer. Small quantities of sample and matrix were individually dissolved in dichloromethane (DCM) or tetrahydrofuran (THF), mixed prior to dropping on a stainless-steel target plate and dried under ambient conditions. Tetracyanoquinodimethane (TCNQ) and 4'-hydroxyazobenzene-2-carboxylic acid (HABA) were used as matrix, providing the same qualitative results. Measurements were performed in positive ion mode. NMR, elemental analysis and HRMS were performed by the Central Institute for Engineering, Electronics and Analytics (ZEA-3), Forschungszentrum Jülich GmbH (52425 Jülich, Germany).

Surface preparation and (SP)-STM/STS experiments were performed in a Joule-Thomson STM system from SPECS Surface Nano Analysis with an integrated superconducting split-coil magnet that generates a magnetic field of up to ±3 T perpendicular to the sample surface. All experiments were performed under UHV conditions (< 1×10^{-10} mbar) at low temperatures (~4 K). Cu(111) single-crystal surfaces were cleaned by repeated sputtering (Ar$^+$, 1500 V, 20 min) and annealing (900 K, 20–30 min). Co was sublimed for two minutes from a rod *via* electron bombardment heating onto the cleaned Cu(111) surface kept at room temperature with a deposition rate of 0.3 ML/min. Immediately after the Co deposition the sample was transferred into the STM and cooled to 4 K to prevent Cu and Co intermixing and to facilitate clean
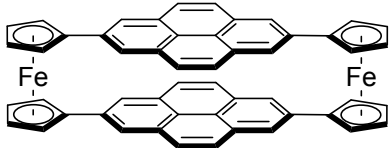
Co nanoisland formation. Prior to molecule deposition, potential hydrogen contaminations were removed by STM tip-induced desorption ($I_t > 25$ nA and $V_b > 750$ mV) as demonstrated by Sicot *et al.*[3,4] Target compounds **1** and **2** were deposited with submonolayer coverage onto the precooled (< 100 K) Co/Cu(111) surface *via* sublimation from a Knudsen cell (530 K, 45 s for **1** and 650 K, 30 s for **2**). All STM/STS experiments were performed with antiferromagnetic Cr tips, prepared by electrochemical etching of Cr wires that were cut from Cr foil (HMW Hauner GmbH, 99.95%).[5] The tips were cleaned *in vacuo* by electron bombardment heating and reshaped during operation where necessary by voltage pulses (5–10 V, 10 ms) to improve the topographic and spin resolving power. Differential conductance dI/dV was measured by superimposing the bias voltage V_b with a sinusoidal modulation voltage ($V_{mod} = 20$ mV, $f_{mod} = 917$ Hz) and detecting the resulting frequency component of the tunneling current at f_{mod} with a lock-in amplifier. Conductance maps dI/d$V(x,y)$ were measured simultaneously with constant-current topography images. V_b is applied to the sample, *i.e.* positive (negative) V_b corresponds to probing unoccupied (occupied) states of the sample.

Syntheses

Synthesis of 2,7-diferrocenylpyrene **1**[6]

[Bpin]$_2$pyrene (0.500 g, 1.1 mmol, 1.0 equiv.), iodoferrocene (1.024 g, 3.3 mmol, 3.0 equiv.), PdCl$_2$(dtbpf) (0.036 g, 0.06 mmol, 0.05 equiv.) and K$_3$PO$_4$ (0.935 g, 4.4 mmol, 4.0 equiv.) were added to a dry Schlenk flask under a stream of Ar. Anhydrous DMF (~25 mL) was added and the reaction mixture was stirred under Ar at 60 °C for 16 h. More catalyst PdCl$_2$(dtbpf) (0.036 g, 0.06 mmol, 0.05 equiv.) was added and the reaction was continued at 60 °C for 48 h. The resulting dark brown suspension was diluted with dichloromethane and water and sonicated for 10 min. Filtration and washing with water, methanol, toluene, and chloroform yielded a brownish orange powder. After sublimation at 300 °C (~6.9×10^{-3} mbar) the product was received as dark orange solid (0.405 g, 65%). Further purification for STM experiments was achieved by gradient sublimation. Elemental analysis after conventional sublimation: Found C, 75.3; H, 4.63. C$_{36}$H$_{26}$Fe$_2$ requires C, 75.82; H, 4.60%; after gradient sublimation: Found C, 75.9; H, 4.59. C$_{36}$H$_{26}$Fe$_2$ requires C, 75.82; H 4.60%; ^{1}H-NMR (600.15 MHz, toluene-d8): δ_H = 8.20 (s, 4H; Py-H), 7.86 (s, 4H; Py-H), 4.80 (pseudo-t, *J* = 1.8 Hz, 4H; Cp-H), 4.27 (pseudo-t, *J* = 1.8Hz, 4H; Cp-H), 3.94 (s, 10H; Cp-H) ppm. HRMS (MALDI): *m/z* calcd. for C$_{36}$H$_{26}$Fe$_2$ [M]$^+$ 570.0733, found 570.0725.

Synthesis of cyclophane **2**

[Bpin]$_2$pyrene (2.000 g, 4.4 mmol, 1.1 equiv.), PdCl$_2$(dtbpf) (0.261 g, 0.4 mmol, 0.1 equiv.) and K$_3$PO$_4$ (3.399 g, 16 mmol, 4.0 equiv.) were added to a dry Schlenk flask under a stream of Ar. 1,1'-Diiodoferrocene (1.753 g, 4.0 mmol, 1.0 equiv.) was dissolved in anhydrous DMF (~200 mL) and cannulated to the reaction mixture. After stirring under Ar at 80 °C for 16 h, more catalyst PdCl$_2$(dtbpf) (0.131 g, 0.2 mmol, 0.05 equiv.) was added and the reaction was continued at 80 °C for 48 h. The resulting brownish suspension was diluted with water and dichloromethane, sonicated for 10 min, filtered, and washed with water, methanol, toluene, and chloroform. After drying under vacuum, the remaining dark brownish solid (~1.5 g) was sublimed at 550 °C (~6.9×10^{-3} mbar) onto a water-chilled cold finger and the raw product was received as reddish orange powder (0.100 g, 6.5%). Further purification was achieved by repeated gradient sublimation and several milligrams of red single crystalline product could be recovered (<1%). Elemental analysis: Found C, 78.9; H, 4.08. C$_{52}$H$_{32}$Fe$_2$ requires C, 81.27; H, 4.20%; HRMS (MALDI): m/z calcd. for C$_{52}$H$_{32}$Fe$_2$ [M]$^+$ 768.1203, found 768.1181. The product is too insoluble for reliable NMR experiments even at elevated temperatures (~100 °C) in 1,2-dichlorobenzene-d4.

Purification by gradient sublimation

Purification for STM studies and single-crystal growth for X-ray diffraction experiments of raw products **1** and **2** were achieved by gradient sublimation as schematically shown in Fig. S1. A quartz glass tube filled with multiple quartz ring segments is inserted into a conical brass tube. The brass tube is heated to a set temperature by a heating element that defines the sublimation zone. The temperature along the brass tube decreases with increasing distance to the heating element, thus a temperature gradient is created that is assessed by thermocouples along the brass tube (T1–T3 in Fig. S1). The molecular sample is inserted into an inner quartz ring at the sublimation zone. Then the quartz tube is evacuated by a turbomolecular vacuum pump to low pressures ($\sim 10^{-4}$ mbar) and a steady Ar ($\geq$ 99.9999%) flow is applied *via* a leak valve. After reaching a suitable temperature at the sublimation zone, the raw product and potential impurities sublime and deposit at different positions of the tube depending on the local temperature and molecular properties such as vapor pressure.[7–9] The use of inner quartz glass rings allows simple and clean removal of the sublimed and re-crystallized products. For crystal growth of **1** the sublimation zone was heated to 300 °C (50 K h^{-1}) for 15 h, followed by natural cooling to room temperature. The temperatures at T2 and T3 were 111 °C and 50 °C, respectively. For crystal growth of **2** the temperature of the sublimation zone was quickly ramped to 300 °C (250 K h^{-1}), slowly increased to 500 °C (10 K h^{-1}; T2 $\approx$ 169 °C and T3 $\approx$ 66 °C), kept for 5 h at 500 °C and then naturally cooled to room temperature. To receive high-quality single crystals the process was repeated twice or thrice using the main fraction from the previous sublimation process.
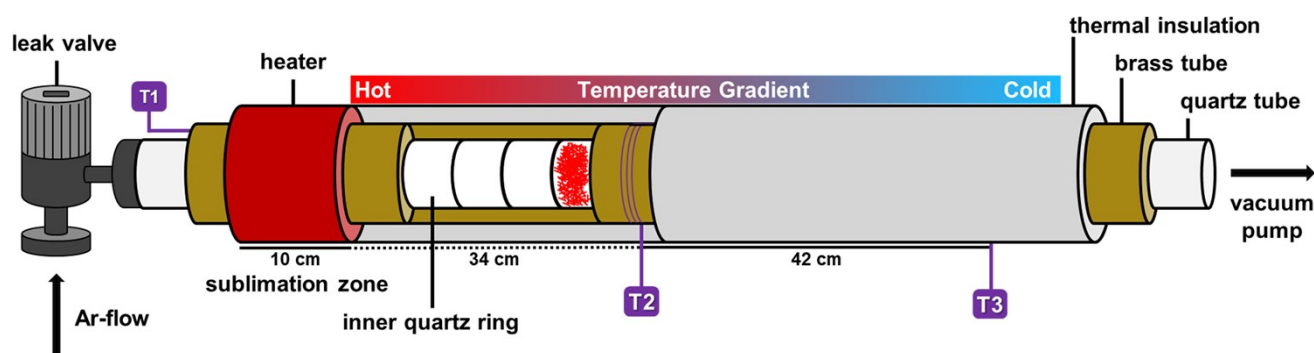

Fig. S1   Schematic representation of the gradient sublimation apparatus used for both purification and single crystal growth of insoluble target compounds **1** and **2**.
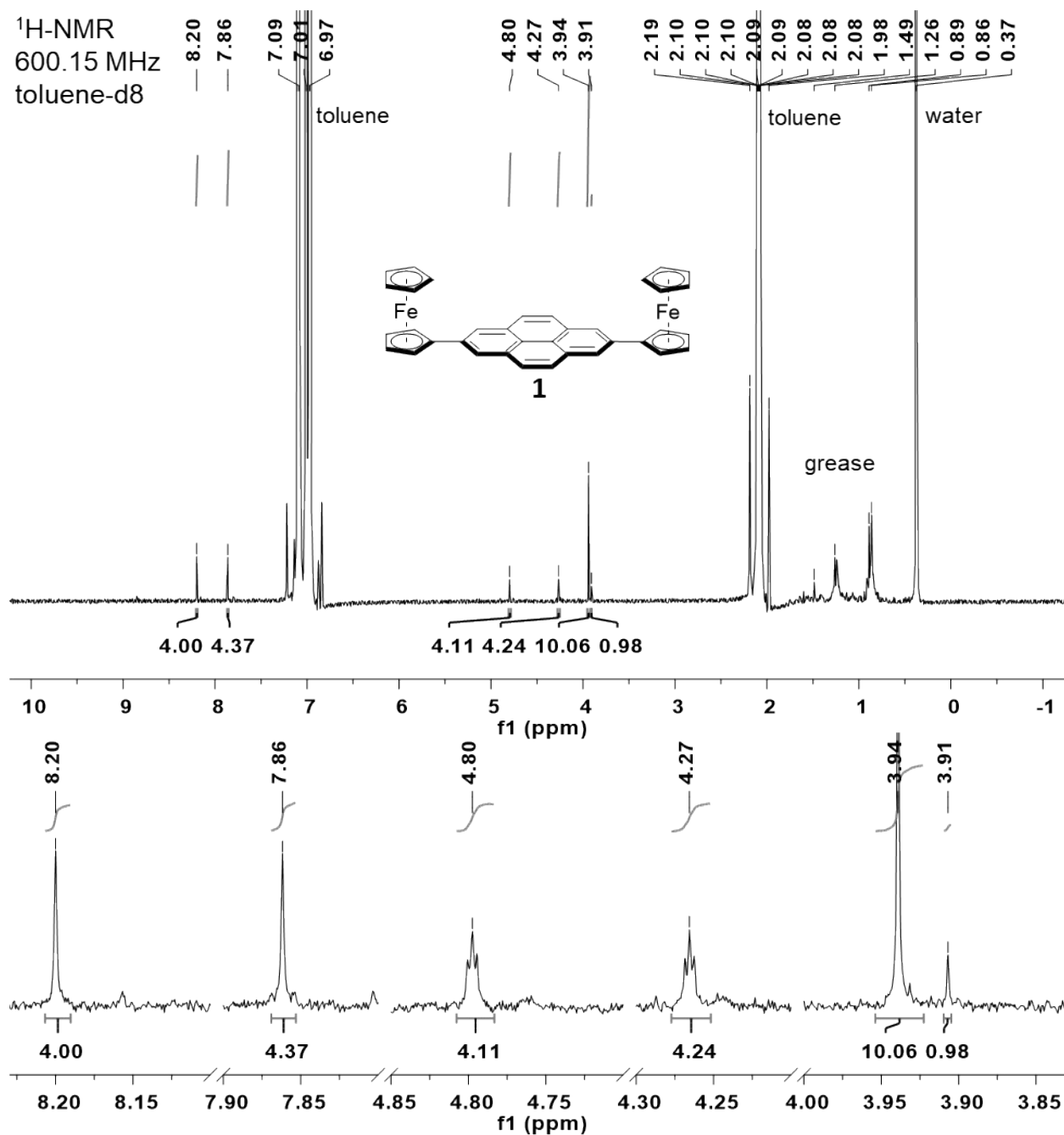
Nuclear magnetic resonance (NMR) spectrum of 1

Fig. S2 ¹H-NMR spectra (600.15 MHz) of **1** measured in toluene-d8 showing every peak (top) and peaks only related to **1** (bottom).
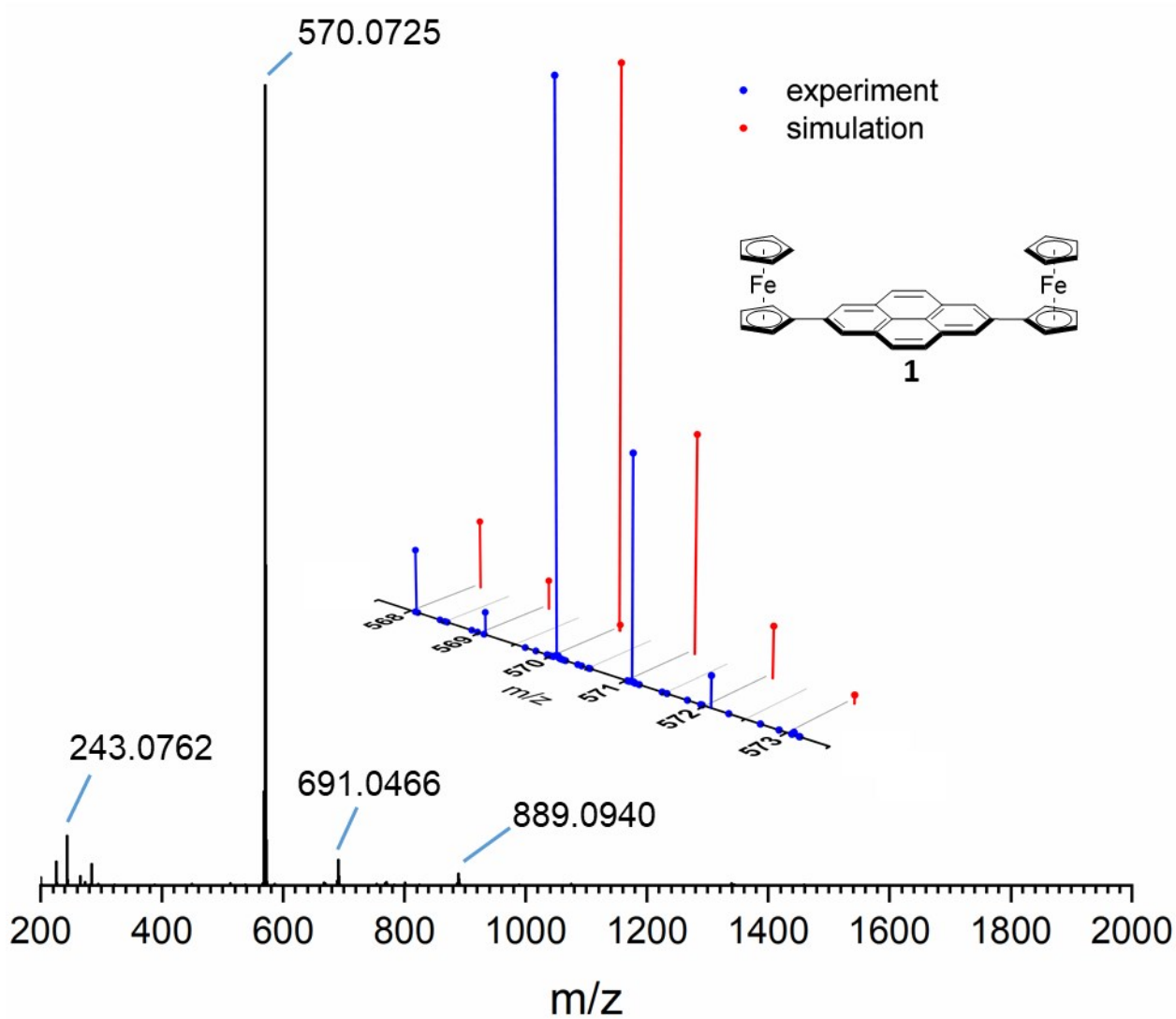
Matrix-assisted laser desorption/ionization (MALDI) high-resolution mass spectrometry (HRMS) data of 1 and 2

Fig. S3   MALDI mass spectrum of 2,7-diferrocenylpyrene **1**; Inset: comparison of the corresponding isotope distribution (blue) with simulated values (red).
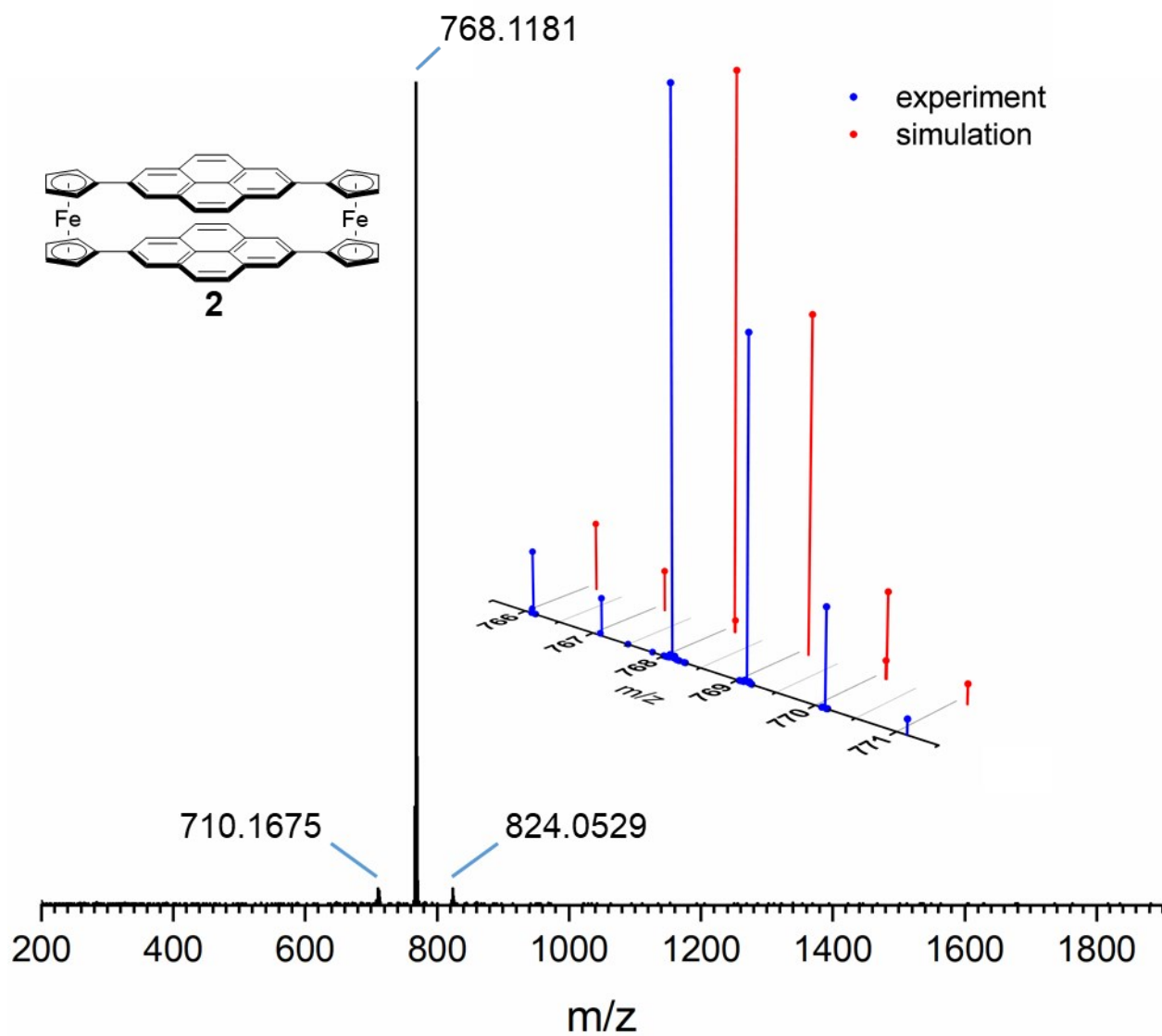
Fig. S4   MALDI mass spectrum of cyclophane **2**; Inset: comparison of the corresponding isotope distribution (blue) with simulated values (red).
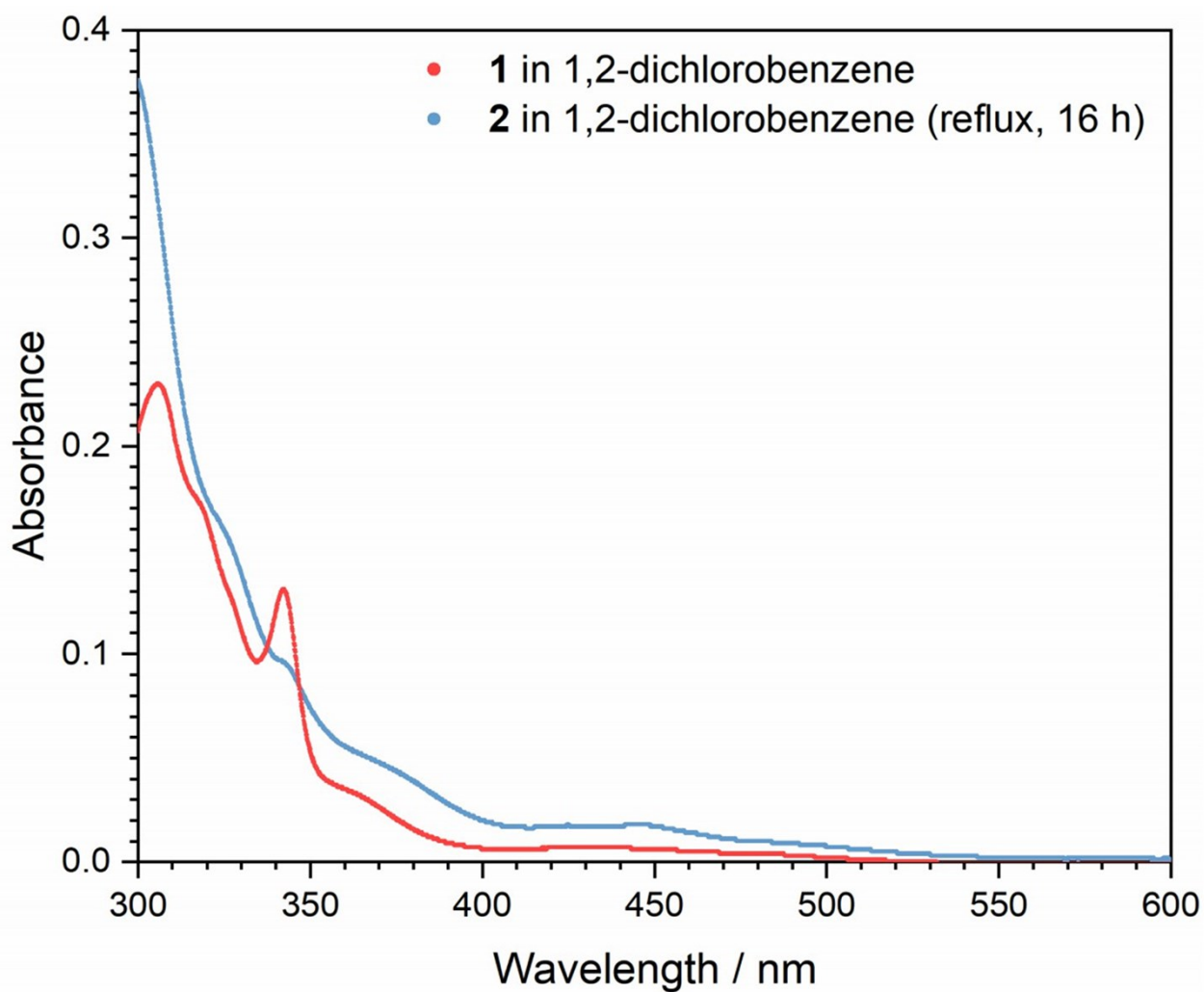
Ultraviolet-Visible (UV-Vis) absorption spectra of **1** and **2**

Fig. S5 UV-Vis spectra of **1** (red) and **2** (blue) recorded in 1,2-dichlorobenzene. Because of the low solubility of **2**, a saturated solution was measured, which was received after refluxing a suspension of **2** in DCB under Ar for 16 h, cooling to room temperature and filtration.

Fourier-transform infrared (FT-IR) spectra of **1** and **2**
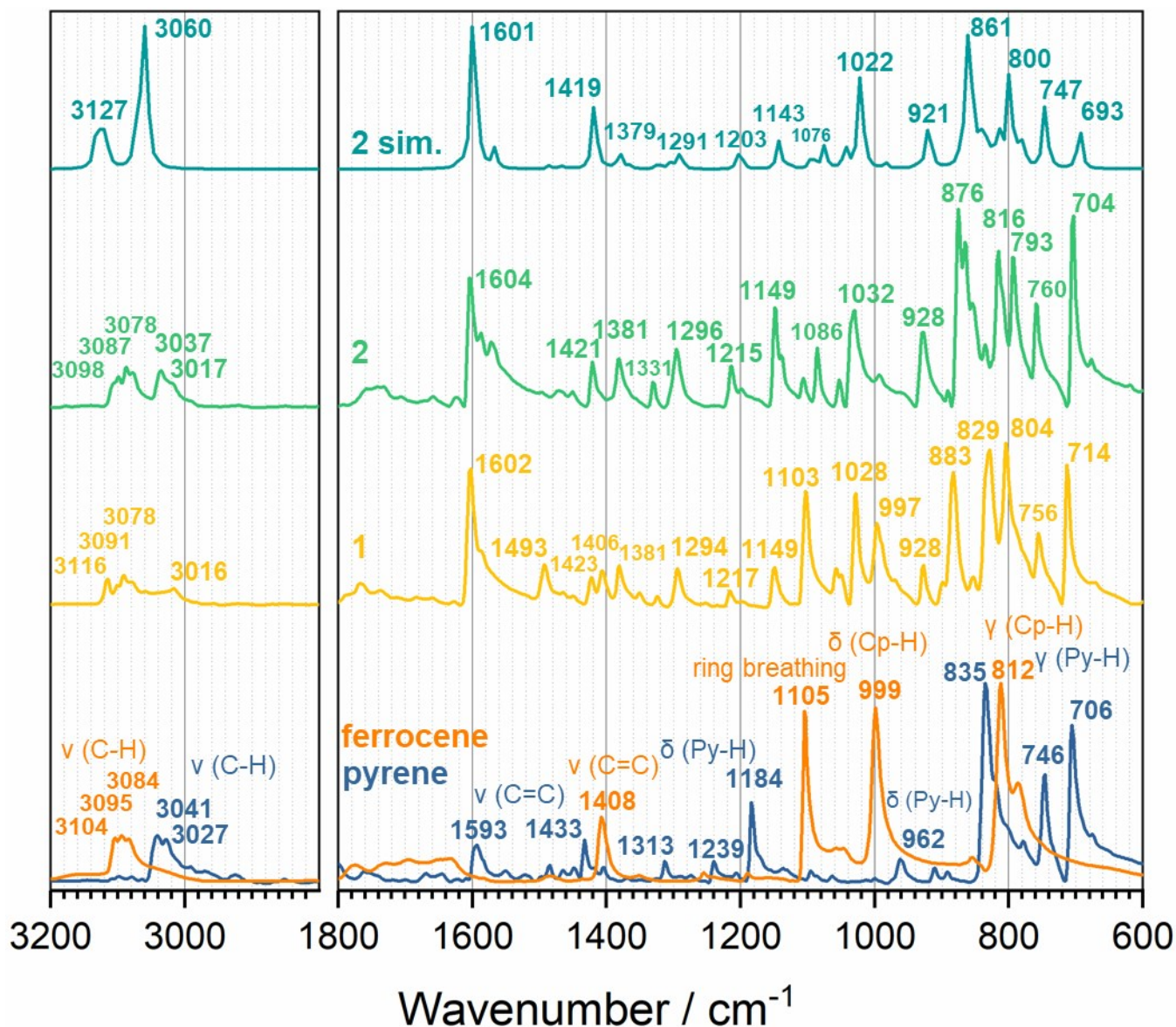
Fig. S6   Normalized FT-IR absorption spectra of **1** (yellow, also see ref [6]) and **2** (green) recorded with an ATR set-up (diamond crystal). A spectrum of **2** has been simulated with DFT (B3LYP-D3-BJ/6-31G(d,p)) and scaled by a factor of 0.961 (dark cyan).[10] Reference spectra of pyrene (blue) and ferrocene (orange) were measured under the same conditions and plotted with vibrational mode assignments according to previous reports.[11-14] ν: stretching; δ: in-plane bending; γ: out-of-plane bending; Cp: cyclopentadienyl; Py: pyrene.

Single-crystal X-ray diffractometry

Single crystals of **1** and **2** were grown by gradient sublimation and mounted on a Hampton Cryoloop using Paratone-N oil. Diffraction data were collected at 299(2) K (**1**) and 101(3) K (**2**) on a SuperNova (Rigaku OD) diffractometer using Mo-Kα radiation (λ = 0.71073 Å). Data reduction and numerical absorption correction (Gaussian integration) were performed using CrysAlisPro.[15]

All structures were solved using SHELXT[16] (intrinsic phasing) and refined by full-matrix least-squares against |F^2| using SHELXL[17] within Olex2 v1.3.[18] Hydrogen atoms were added geometrically and refined using a riding model. Relevant crystallographic information for **1** and **2** are summarized in Table S1 and supplementary crystallographic data are provided free of charge by the joint Cambridge Crystallographic Data Centre (CCDC) and Fachinformationszentrum (FIZ) Karlsruhe Access Structures service https://www.ccdc.cam.ac.uk/structures (CCDC deposition numbers *2056849* (**1**) and *2056848* (**2**)). Crystal and molecular structures were visualized with CrystalMaker X.[19] Bending angles of pyrene were determined according to Ghasemabadi *et al.*[20] by calculating the smallest angle between two planes that are defined by the carbon atoms of pyrene C1, C2 and C3, and C6, C7 and C8, respectively.
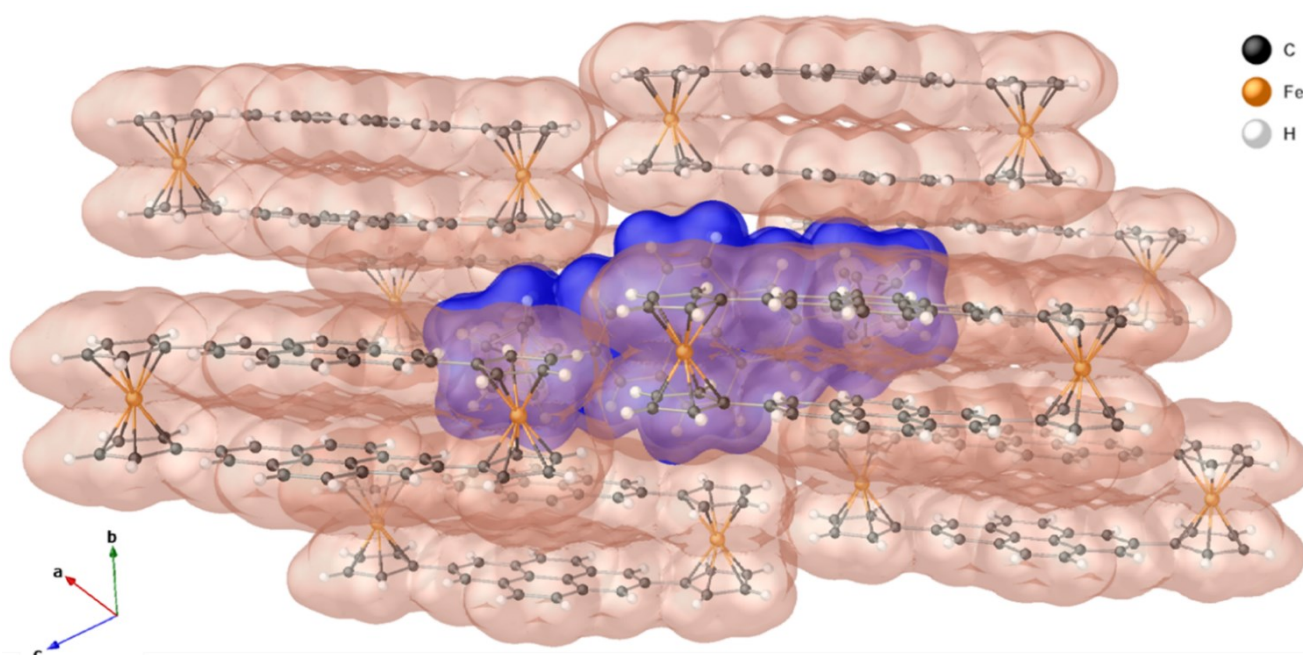

Fig. S7   Representation of the crystal packing of **2** showing that a central molecule (blue) interacts with eight surrounding molecules (red) *via* C-H···π stacking. All molecules are plotted with van der Waals surfaces according to the values reported by Bondi[21] as implemented in CrystalMaker X.[19]

Table S1   Crystallographic information for **1** and **2**.

	Compound **1**	Compound **2**
empirical formula	$C_{36}H_{26}Fe_2$	$C_{52}H_{32}Fe_2$
formula weight / g mol^{-1}	570.27	768.47
crystal size / mm	0.206 × 0.128 × 0.048	0.109 × 0.068 × 0.039
crystal system	monoclinic	monoclinic
space group	$P\,2_1/c$	$P\,2_1/c$
a / Å	11.1819(4)	10.6986(3)
b / Å	7.9345(2)	10.1128(2)
c / Å	14.5190(5)	15.0273(4)
β / °	100.936(3)	94.840(2)
V / Å^3	1264.77(7)	1620.05(7)
Z	2	2
ρ_{calcd} / g cm^{-3}	1.497	1.575
μ / mm^{-1}	1.172	0.938
$F(000)$	588.0	792.0
T / K	299(2)	101(3)
radiation	Mo Kα (λ = 0.71073 Å)	Mo Kα (λ = 0.71073 Å)
2Θ range for data collection	6.654° to 48.21°	6.324° to 58.592°
index ranges	−12 ≤ h ≤ 12, −9 ≤ k ≤ 9, −16 ≤ l ≤ 16	−14 ≤ h ≤ 14, −13 ≤ k ≤ 13, −19 ≤ l ≤ 19
reflections collected	21230	34892
independent reflections	1998 [R_{int} = 0.0961, R_{sigma} = 0.0559]	4196 [R_{int} = 0.1170, R_{sigma} = 0.0857]

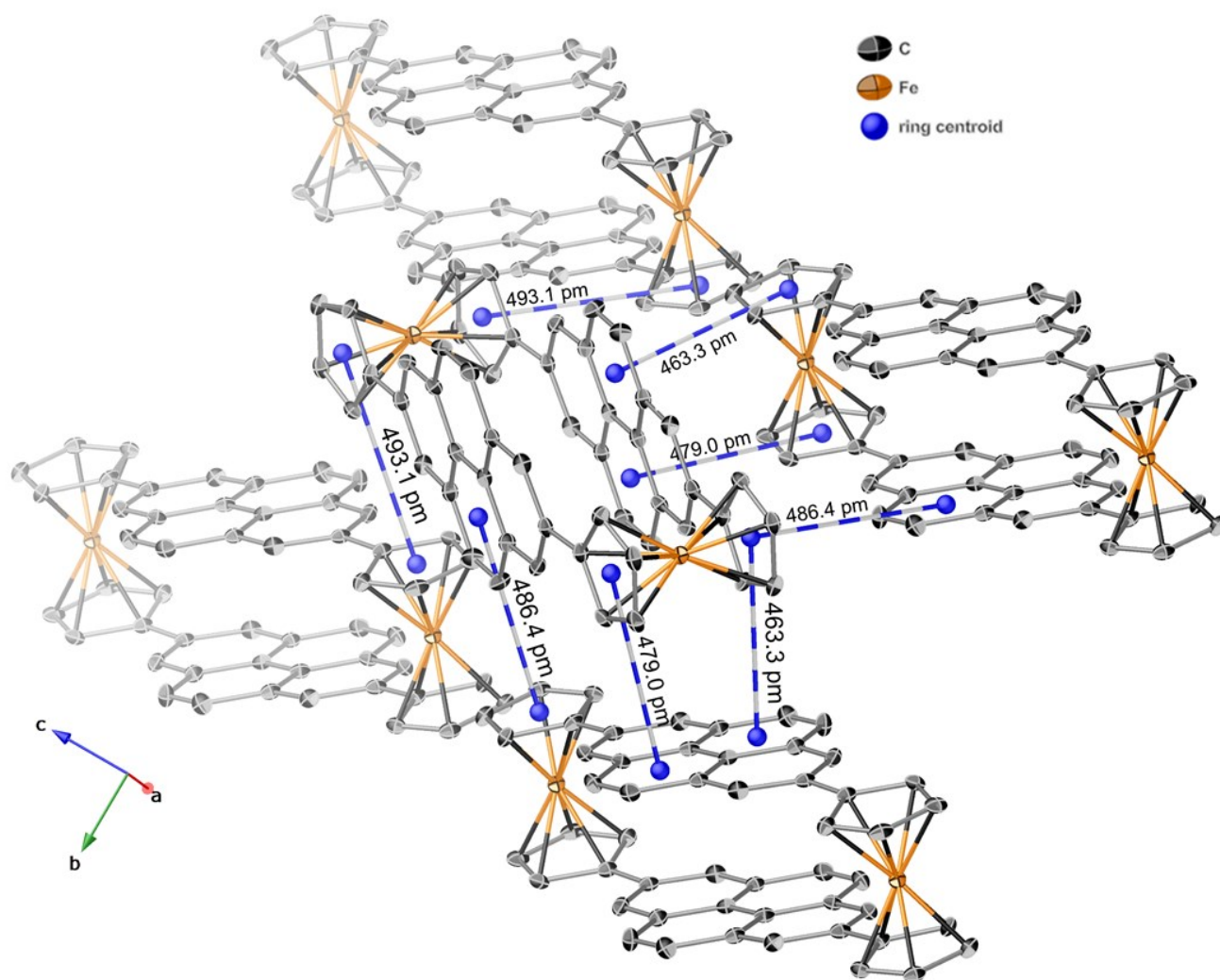| data/restraints/parameters	1998/0/172	4196/0/244
Goodness-of-fit on F^2	1.050	1.025
final R indexes [I ≥ 2σ(I)]	$R_1 = 0.0402$, $wR_2 = 0.0695$	$R_1 = 0.0483$, $wR_2 = 0.0964$
final R indexes [all data]	$R_1 = 0.0679$, $wR_2 = 0.0829$	$R_1 = 0.0968$, $wR_2 = 0.1180$
largest diff. peak/hole / e Å^{-3}	0.51/–0.24	0.65/–0.52

Fig. S8 Crystal packing of cyclophane **2** showing relevant intermolecular interactions between aromatic ring centroids (blue) as indicated by blue-gray lines with corresponding distances. Molecules are displayed with thermal ellipsoids (50% probability). Other surrounding molecules and hydrogen atoms are omitted for clarity.

Scanning tunneling microscope (STM) tip-induced molecule modification

In order to probe the origin of the instability of the investigated molecules (**1** and **2**) on Co/Cu(111), we studied the asymmetrically appearing molecules that were frequently observed after STM imaging at elevated voltages ($|V_b| > 1$ V) and currents ($|I_t| > 100$ pA). These fragments exhibit similar lateral dimensions as intact molecules, but a significantly lower apparent height (~180 pm) at one of the two Fc sites (Fig. 3, S9 and S10). While an alternate adsorption geometry, tilting of one Fc group, or higher oxidation state of Fe within Fc in comparison with the intact molecules cannot be ruled out, the presence of these species is most likely caused by C-C and Fe-C bond breakage and release of cyclopentadienyl (Cp) and Py, or Cp-Py. Fragmentation of Fc groups into Cp and FeCp units after deposition of unfunctionalized Fc onto Au,[22] Pt[23,24] and Cu[25,26] surfaces has previously been observed by other authors. In this context Zhong *et al*. demonstrated that one Cp ring of Fc groups within a tetradecylene-bridged di-ferrocene molecule adsorbed on Cu(110) can be systematically removed *via* STM tip manipulation. The resulting CpFe complex is characterized by a reduced surface mobility due to increased molecule-metal interactions and shows a magnetic moment of 1.86 μ_B concentrated on the Fe atom.[25]

Therefore, we performed controlled current-induced molecule modification by placing an STM tip first over a Co island while applying a bias voltage $|V_b| > 1$ V (at $I_t = 50$–100 pA) and then moving it over one of the two Fc units of **1** or **2** (Fig. S9 and S10). After a few seconds, an abrupt, irreversible apparent height reduction by 30–50% (dependent on V_b and I_t used for imaging) was observed that corresponds well with the results reported by Zhong *et al*.[25] The resulting modified molecules are rotated by 20° and are identical to the fragments sporadically observed after deposition of both **1** and **2** on Co. In contrast to the previous report,[25] in which a voltage between 2.2–2.5 V was needed to remove the Cp ring, we could observe this modification on Co already at much lower voltages, which is not surprising considering the expected higher strength of molecule-surface interaction on reactive Co/Cu(111) in comparison to Cu(110).

Largely similar changes of the topographic images of molecules **1** and **2** after intentional modification suggest identical final fragments. The removal of a Cp ring from **1** does not involve C-C bond breakage and should follow a similar mechanism as found in Fc. For cyclophane **2** the removal of Cp requires breakage of a covalent Cp-Py bond in conjunction with the release of Py or Py-Cp fragments. Note that the two fragmentation experiments in Fig. S10 were performed with different tips, possibly providing different lateral resolution that may affect the profile shapes but hardly the observed modification-induced height changes. Unfortunately, no removed fragments, which are probably too mobile even on Co, could be clearly identified after successful STM tip manipulation. Further in-depth investigations are necessary to elucidate the involved mechanism.
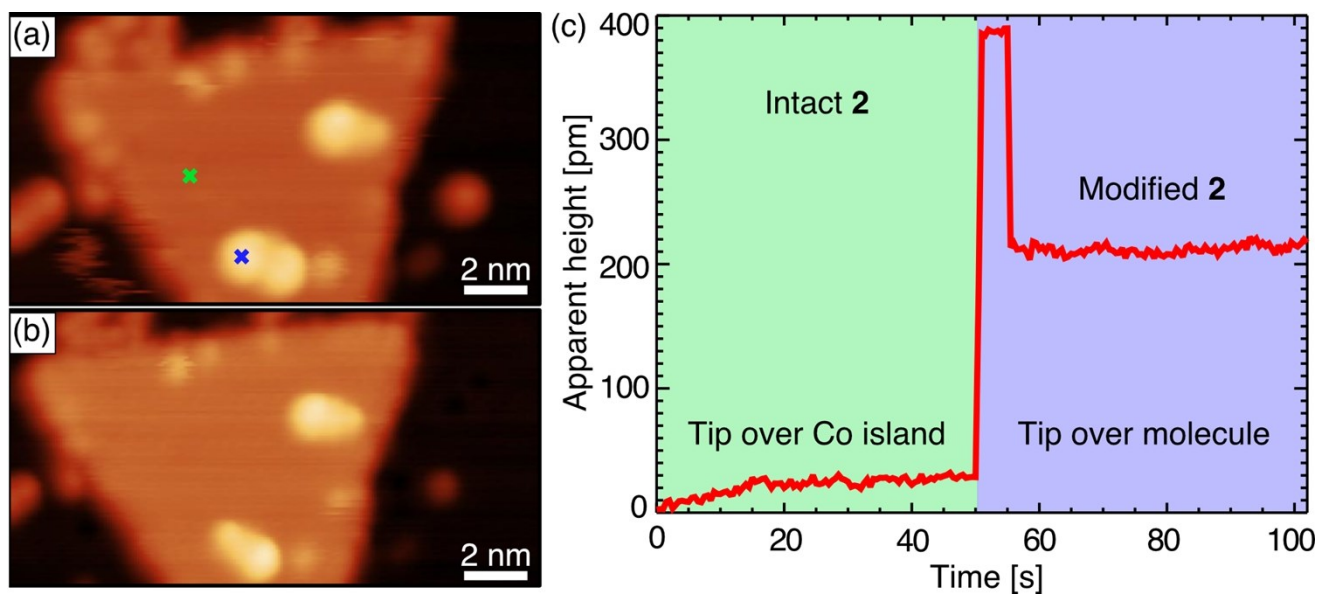
Fig. S9 Topographic constant-current STM images (a) before ($V_b = 2$ V, $I_t = 50$ pA) and (b) after ($V_b = 0.5$ V, $I_t = 50$ pA) intentional current-induced modification of a cyclophane **2** on Co(111). (c) Time trace of the apparent height at $V_b = 1.5$ V and $I_t = 50$ pA taken while the tip was first positioned on the Co nanoisland at the green cross in (a) and then moved to the Fc site of the molecule **2** at the lower image edge marked by a blue cross. After ~3 s at the Fc site, an abrupt height change indicates the modification of the molecule.
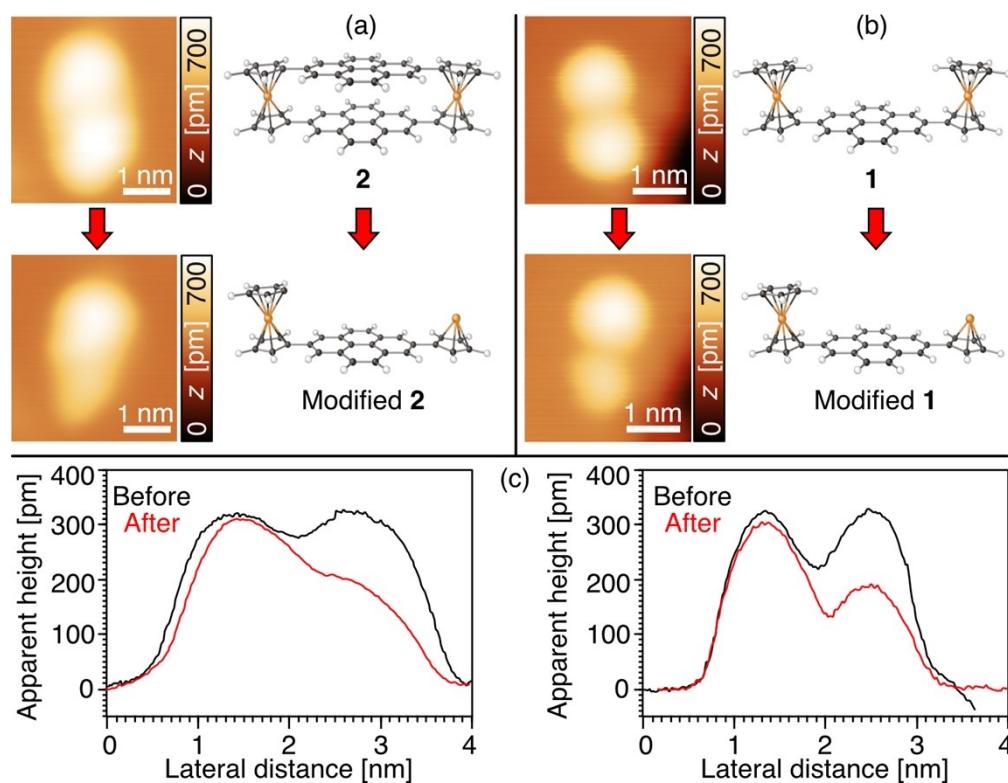
Fig. S10 Current-induced modification of (a) cyclophane **2** and (b) reference molecule **1** on Co/Cu(111), induced by applying $V_b = 3$ V and $I_t = 100$ pA for **2** and $V_b = 2$V and $I_t = 50$ pA for **1**. The upper part shows topographic images before and after the modifications with the proposed fragmentation process schemes. (a): $V_b = 0.5$ V, $I_t = 100$ pA before and $V_b = -0.5$ V, $I_t = 100$ pA after; (b): $V_b = 1.5$ V, $I_t = 50$ pA before and $V_b = -2$ V, $I_t = 50$ pA after modification. (c) Cross-sections along the longitudinal axes of the molecules shown in (a) and (b) reveal a similar change of the apparent height at the modified Fc site.

Spatial distribution of spin polarization measured by spin polarized (SP) STM/STS

We employed spin-polarized scanning tunneling microscopy and spectroscopy (SP-STM/STS) to investigate the magnetic properties of molecule **2** chemisorbed on Co nanoislands. The spatial distribution of the spin polarization above an adsorbed molecule at energies close to the Fermi energy is accessed by measuring differential conductance maps for parallel and antiparallel alignment of the magnetizations of tip and substrate (here the Co nanoisland).

According to the generalized Tersoff-Hamann model for electron tunneling in the STM configuration,[27,28] the differential conductance is given by

$$\frac{dI}{dV} \propto n_T n_S + \vec{m}_T \cdot \vec{m}_S,$$

where n_T and n_S are the local densities of states (DOS) of tip (T) and sample (S) at the position of the STM tip, and $\vec{m}_T$ and $\vec{m}_S$ are the corresponding local magnetization densities

$$\vec{m}_i = \left(n_i^\uparrow - n_i^\downarrow\right)\vec{e}_i = P_i n_i \vec{e}_i \quad ; \quad i = T, S.$$

Here, $n_i^\uparrow$ and $n_i^\downarrow$ denote the majority and minority spin DOS of tip and sample, and $\vec{e}_i$ are unit vectors in the directions of the respective magnetizations. $n_i = n_i^\uparrow + n_i^\downarrow$ are the total DOS, P_i the spin polarizations. If the conductance is measured for parallel (P) and antiparallel (AP) alignment of tip and sample magnetizations, $\left(\frac{dI}{dV}\right)_P$ and $\left(\frac{dI}{dV}\right)_{AP}$, the spin asymmetry A, defined as

$$A = \frac{\left(\frac{dI}{dV}\right)_P - \left(\frac{dI}{dV}\right)_{AP}}{\left(\frac{dI}{dV}\right)_P + \left(\frac{dI}{dV}\right)_{AP}}, \tag{S1}$$

is directly related to the spin polarizations P_T and P_S,

$$A = P_T P_S. \tag{S2}$$

However, neither the tip magnetization magnitude (P_T) nor the exact tip magnetization axis ($\vec{e}_T$) are *a priori* known for a given tip and thus need to be determined and calibrated (*vide infra*). Since the magnetic state of the tip (P_T and $\vec{e}_T$) is constant during the acquisition of a spin asymmetry map $A(x,y)$, any variation in $A(x,y)$ is due to laterally different spin polarization of the sample, $P_S(x,y) \propto A(x,y)$.
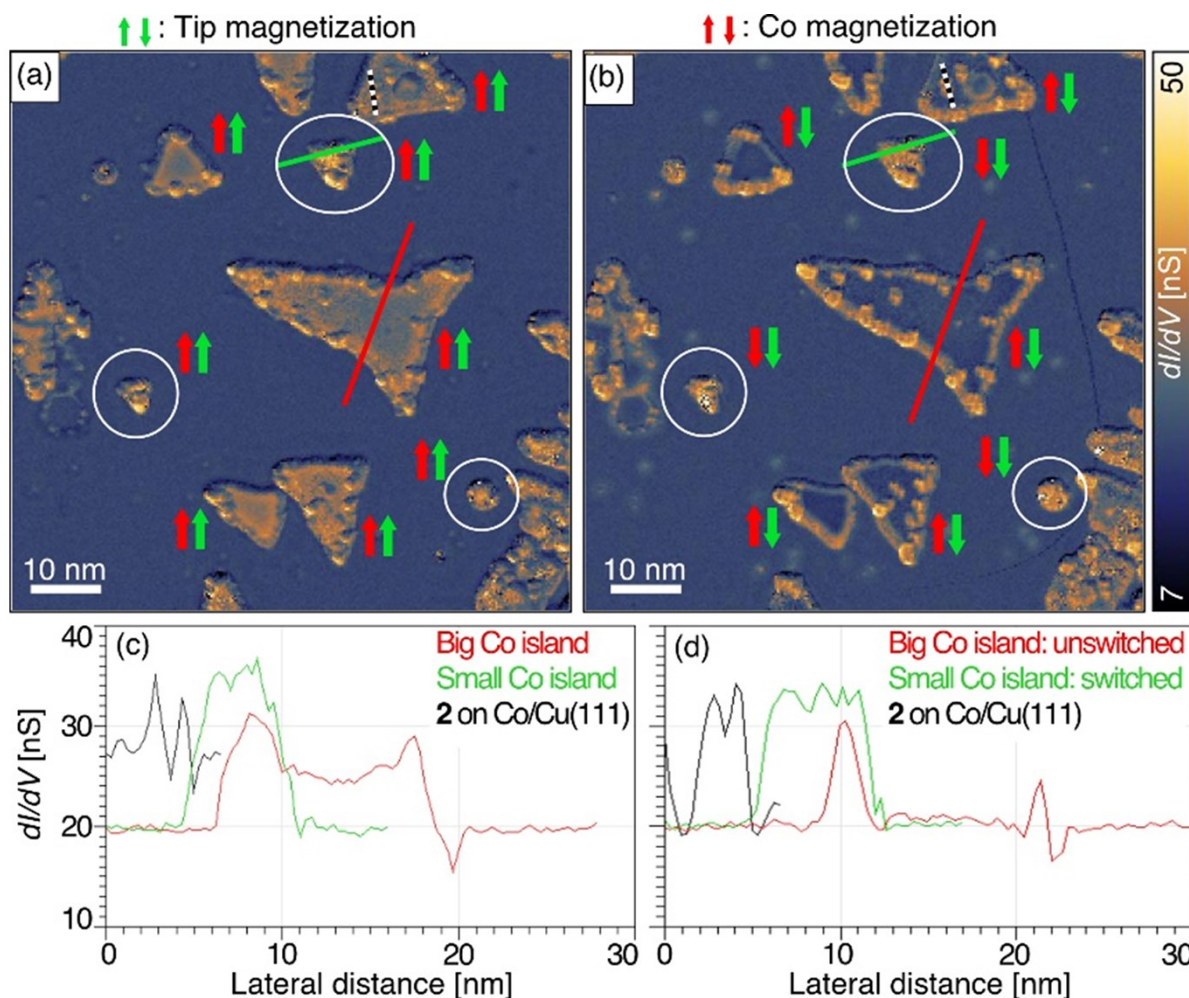
Fig. S11 Conductance maps of Co nanoislands partly covered with molecule **2**. (a) is measured in the saturated magnetic state in a field of +1 T and (b) after sweeping the field to −1 T. Pairs of red and green arrows indicate for each island the alignment of tip (green) and island (red) magnetization. Islands in white ellipses have a switching field less than ±1 T and reverse their magnetization from (a) to (b), as does the tip. (c),(d) Profiles across various islands as indicated by correspondingly colored lines in (a) and (b), respectively.

In our experiments, the relative alignment of tip and nanoisland magnetizations can be controlled by an external field of up to ±3 T that is applied in the STM during operation perpendicular to the sample surface. Triangular double-layered Co nanoislands on Cu(111) with out-of-plane magnetization prepared in the same manner as described above exhibit size-dependent coercivity and reverse magnetization at switching fields between 0.2 T for smallest islands (~700 Co atoms, ~20 nm^2, ~6 nm edge length) and about 2.4 T for islands containing 5500 Co atoms (~155 nm^2, ~19 nm edge length).[29] Larger islands remagnetize *via* domain wall formation and are not used in this study. STM tips made from bulk Cr, as in this work, or by coating a W tip with a thin Cr film have been shown to reveal a magnetization reversal at a field of the order or 0.5 T. This is explained by uncompensated spins at the very apex of the tip that are sensitive to the external field.[30,31] The different switching fields of tip and Co nanoislands allow external control of the

relative magnetization alignment: P alignment is obtained by applying a saturating field exceeding both switching fields and AP alignment by sweeping the field from positive saturation to a negative value between the two switching field values.

Fig. S11 shows two conductance maps at $V_b = -500$ mV of several Co nanoislands partly covered with molecule **2**. After applying a saturating field in positive direction, first Fig. S11a was measured at a field of +1 T and then Fig. S11b after sweeping the field to −1 T. Pairs of green and red arrows next to islands indicate the alignment of tip (green) and island (red) magnetization for this specific island. In Fig. S11a, both tip and all islands retain the saturated state, and the magnetization of the tip is parallel to the magnetization of all nanoislands. In Fig. S11b, the magnetization of the tip is reversed because the external field of −1 T exceeds the switching field of the tip of −0.5 T. This leads for the big islands with a switching field larger than ±1 T to a change of the relative alignment of tip and sample magnetizations, as can be clearly seen by the strong change of contrast in the interior of the islands (red profiles in Fig. S11c,d). Small islands with a switching field below ±1 T (white ellipses in Fig. S11a,b) have also reversed their magnetizations. Here, both tip and sample magnetizations now point in the negative field direction, but their relative alignment remains parallel, and the contrast is unchanged (green profiles in Fig. S11c,d).
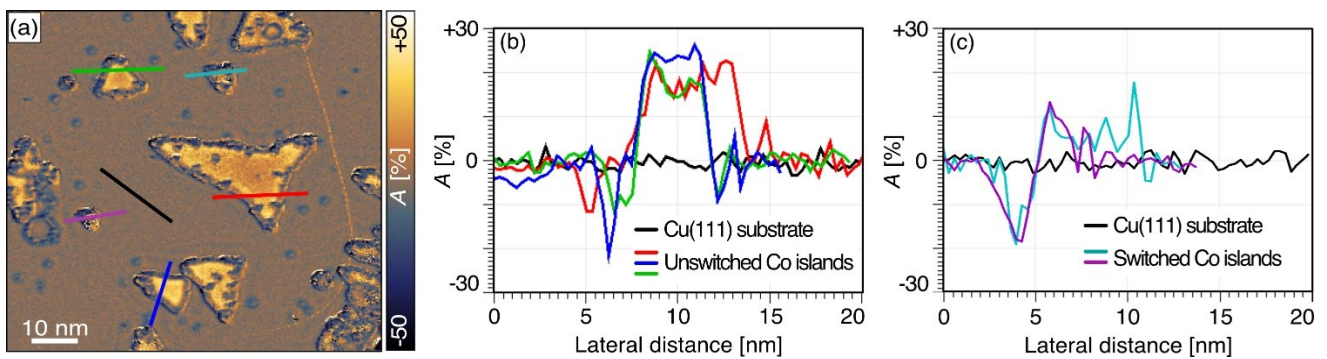

Fig. S12 (a) Spin asymmetry map calculated according to Equation (S1) from the data in Fig. S11. (b),(c) Profiles across various islands as indicated by correspondingly colored lines in (a).

Fig. S12a shows the spin asymmetry map calculated from the data in Fig. S11 according to Equation (S1). The big islands appear bright indicating the magnetization reversal of the tip, whereas the nonmagnetic Cu substrate yields a vanishing spin asymmetry $A \approx 0$. The contrast at the edges of the islands, which renders the small islands visible at all, is due to spin-polarized edge states[32] and inevitable cross-talk between topography and spin asymmetry. The profiles in Fig. S12b,c indicate a spin asymmetry of about 20% for big Co islands that have not reversed their magnetization during the field sweep from +1 to −1 T (red, blue, green in Fig. S12b). Their magnetizations at +1 and −1 T are P and AP aligned, respectively, to the tip magnetization. The small islands (light blue and purple in Fig. S12c) have their magnetization always

parallel to the tip magnetization, and $A \approx 0$ in the interior of the islands. The agreement and consistency of these data with the known and expected magnetic behavior of Co nanoislands on Cu(111) prove the spin resolving power ($P_T \neq 0$) of the Cr tip and show that its axis of spin sensitivity is perpendicular to the surface ($\vec{e}_T \perp$ surface). This kind of tip calibration obtained from imaging a known magnetization distribution is a prerequisite for the investigation of the unknow magnetization profile of chemisorbed cyclophane molecules **2** on Co nanoislands. Two molecules **2** are adsorbed on the larger triangular Co nanoisland at the top edge of the imaged area in Fig. S11 and S12 (see black/white dashed lines and black profiles in Fig. S11). This island is big enough to belong to the unswitched islands. Hence, the spin asymmetry $A(x,y)$ calculated on this island according to Equation (S1) directly reflects the distribution of the polarization above the sample $P_S(x,y)$, see Equation (S2). An enlarged image of the island with the two adsorbed molecules **2** is shown in Fig. 5 of the main text and discussed there in detail.

Computational Methods

Electronic structure and frequency calculations were performed using Density Functional Theory (DFT) employing Gaussian 16 Rev. A.03[33] or Gaussian 09 Rev. D.01[34] software packages in tandem with GaussView 6 or 5, respectively.[35] The Becke three-parameter hybrid, Lee-Yang-Parr correlation functional (B3LYP)[36–40] has been employed with the Pople-style basis set 6-311G(2d) or 6-31G(d,p).[41–45] The empirical dispersion correction developed by Grimme (DFT-D$_3$[46]) with Becke-Johnson (BJ) damping[47,48] has been used as implemented in Gaussian 16 to account for intramolecular vdW interactions for some of these calculations. Molecular orbitals (MOs) were visualized using VMD[49] or GaussView.[35]

The frontier molecular orbitals of cyclophane **2** are depicted in Fig. S13. The amplitudes of these orbitals are localized on either the pyrene or ferrocene groups, with no frontier orbitals having substantial amplitude on both. The orbitals that are localized to the pyrene stack (left side of Fig. S13) clearly derive from combinations of the pyrene HOMO and LUMO, both of which have nodes at the 2- and 7-positions. The orbitals that are localized to the ferrocene groups (right side of Fig. S13) derive directly from the orbitals of isolated ferrocene molecules. For this calculation, D_{2h} point group symmetry was enforced and the structure was optimized to an energy minimum.

A correlation diagram that illustrates the characters of the frontier orbitals of cyclophane **2** is depicted in Fig. S14. The optimized structure of **2**, as presented in Fig. S13, lies at the center of Fig. S14, and all other structures of Fig. S14 take their coordinates from **2**. To the left in Fig. S14, two ferrocene groups at the distance found by optimizing cyclophane **2** have frontier orbital energies that are nearly identical to those of the ferrocene-derived orbitals of **2** and also barely distinguishable from the energies of the frontier orbitals of ferrocene in isolation. To the right of cyclophane **2** in Fig. S14, the frontier orbitals of the pyrene stack are shown to have energies that are not perturbed by their bonding to the two ferrocene groups. Instead, the frontier orbitals of the pyrene stack are split by through-space interaction with each other.

The dependence of the through-space coupling energy between pyrene groups upon their orientation is depicted in Fig. 1 of the main text. This figure was constructed from a series of single-point calculations in which two pyrene groups (coordinates optimized in a calculation on isolated pyrene) were set in a fully-eclipsed arrangement with the interplanar spacing determined from the X-ray crystal structure of **2**. The offsets were created by shifting one pyrene group in steps of ~28 pm toward the AB arrangement while holding the interplanar spacing constant. The AB arrangement occurs at a lateral offset of ~280 pm, *i.e.* ten such steps. For this calculation, the dispersion correction was not used and the pyrene dimer structures were not optimized.
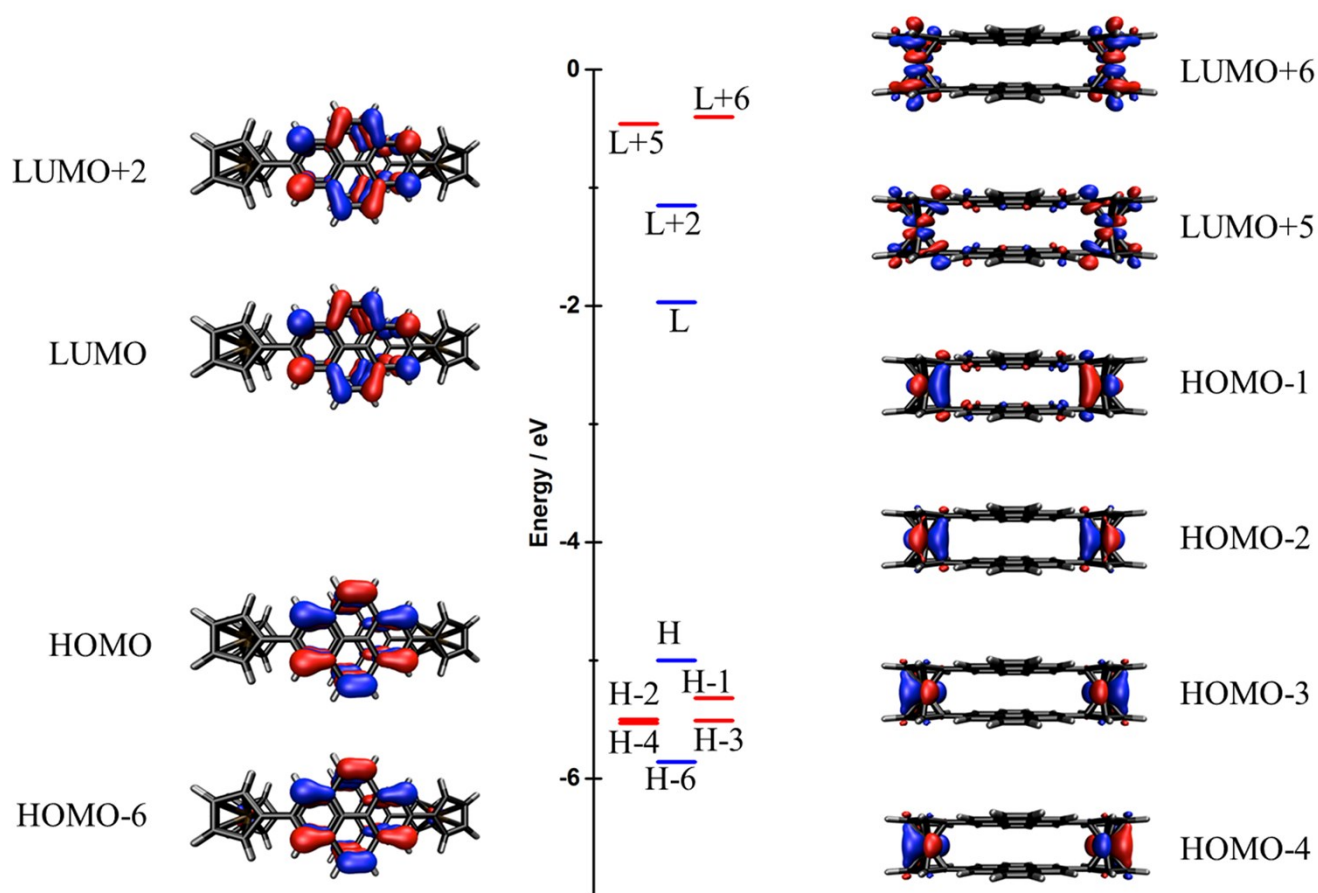
Fig. S13   Energy-level diagram and corresponding molecular orbital isosurfaces of cyclophane **2** (idealized structure with an interplanar distance of ~330 pm and D_{2h} symmetry) showing that the wavefunctions localize on either pyrene (blue line) or ferrocene (red line) subunits. These calculations were performed using DFT (B3LYP/6-311G(2d) with GD3-BJ dispersion correction. MOs were plotted with isodensity values of +0.02 (blue) and –0.02 (red).
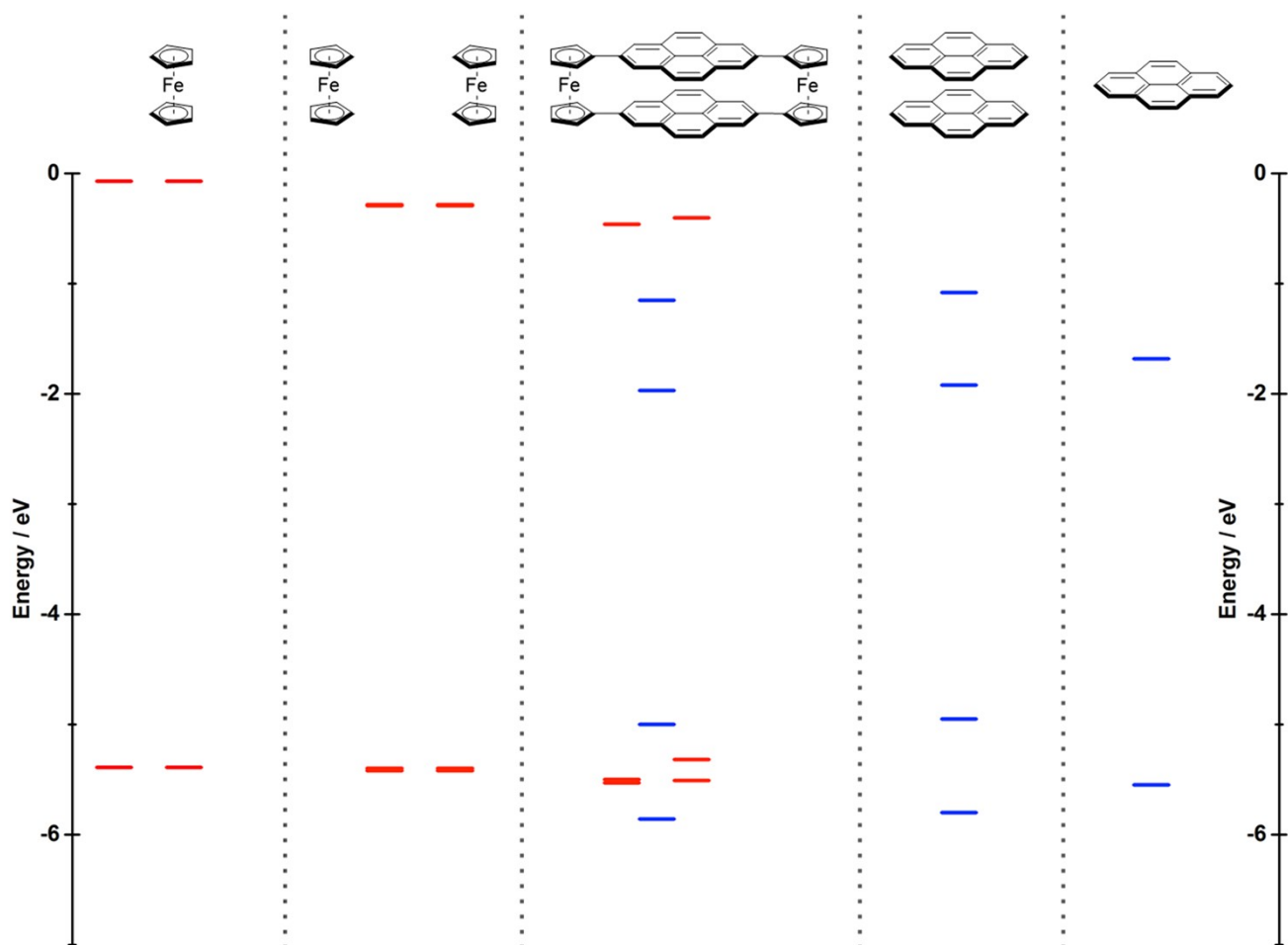
Fig. S14   Correlation diagram for cyclophane **2** (idealized structure with an interplanar distance of ~330 pm and *D*$_{2h}$ symmetry). Single-point energies were calculated using DFT (B3LYP/6-311G(2d)). A blue bar indicates that the corresponding MO is localized on the pyrene groups and red indicates localization on the ferrocene subunits. The orientations and distances of the ferrocene and pyrene pairs are unchanged from the cyclophane structure **2** in the central column.

References

1   A. G. Crawford, Z. Liu, I. A. I. Mkhalid, M. H. Thibault, N. Schwarz, G. Alcaraz, A. Steffen, J. C. Collings, A. S. Batsanov, J. A. K. Howard and T. B. Marder, *Chem. - Eur. J.*, 2012, **18**, 5022-5035.

2   M. Roemer and C. A. Nijhuis, *Dalton Trans.*, 2014, **43**, 11815-11818.

3   M. Sicot, O. Kurnosikov, O. A. O. Adam, H. J. M. Swagten and B. Koopmans, *Phys. Rev. B*, 2008, **77**, 035417.

4   M. Sicot, O. Kurnosikov, H. J. M. Swagten and B. Koopmans, *Surf. Sci.*, 2008, **602**, 3667-3673.

5   A. L. Bassi, C. S. Casari, D. Cattaneo, F. Donati, S. Foglio, M. Passoni, C. E. Bottani, P. Biagioni, A. Brambilla, M. Finazzi, F. Ciccacci and L. Duò, *Appl. Phys. Lett.*, 2007, **91**, 173120.

6   A. Preuß, S. Notz, E. Kovalski, M. Korb, T. Blaudeck, X. Hu, J. Schuster, D. Miesel, T. Rüffer, A. Hildebrandt, K. Schreiter, S. Spange, S. E. Schulz and H. Lang, *Chem. - Eur. J.*, 2020, **26**, 2635-2652.

7   N. T. Morgan, Y. Zhang, E. J. Molitor, B. M. Bell, R. J. Holmes and E. L. Cussler, *AlChE J.*, 2014, **60**, 1347-1354.

8   N. T. Morgan, Y. Zhang, M. L. Grandbois, B. M. Bell, R. J. Holmes and E. L. Cussler, *Org. Electron.*, 2015, **24**, 212-218.

9   J. D. Virdo, A. J. Lough and T. P. Bender, *Acta Crystallogr. Sect. C: Struct. Chem.*, 2016, **72**, 297-307.

10 Computational Chemistry Comparison and Benchmark DataBase (CCCBDB), NIST Standard Reference Database 101, release 21, August 2020, III.B.3.a. (XIII.C.1.); Editor: Russell D. Johnson III; https://cccbdb.nist.gov/vibscalejust.asp (accessed: 2020-10-14)

11 E. R. Lippincott and R. D. Nelson, *Spectrochim. Acta*, 1958, **10**, 307-329.

12 N. Mohammadi, A. Ganesan, C. T. Chantler and F. Wang, *J. Organomet. Chem.*, 2012, **713**, 51-59.

13 S. Califano and G. Abbondanza, *J. Chem. Phys.*, 1963, **39**, 1016-1023.

14 A. Bree, R. A. Kydd, T. N. Misra and V. V. B. Vilkos, *Spectrochim. Acta Part A*, 1971, **27**, 2315-2332.

15 *CrysAlisPro*, Version 1.171.39.46 (**1**) 1.171.40.53 (**2**), Rigaku Oxford Diffraction/Agilent Technologies UK Ltd, Yarnton (UK), 2018 (**1**), 2019 (**2**).

16 G. Sheldrick, *Acta Crystallogr. Sect. A: Found. Adv.*, 2015, **71**, 3-8.

17 G. Sheldrick, *Acta Crystallogr. Sect. C: Struct. Chem.*, 2015, **71**, 3-8.

18 O. V. Dolomanov, L. J. Bourhis, R. J. Gildea, J. A. K. Howard and H. Puschmann, *J. Appl. Crystallogr.*, 2009, **42**, 339-341.

19 D. Palmer, A. Fernandez, M. Gao, *CrystalMaker X Version 10.4.6*, Program for Visualizing Crystal and Molecular Structures, CrystalMaker Software Ltd., Oxfordshire (UK), 2019.

20 P. G. Ghasemabadi, T. Yao and G. J. Bodwell, *Chem. Soc. Rev.*, 2015, **44**, 6494-6518.

21 A. Bondi, *J. Phys. Chem.*, 1964, **68**, 441-451.

22 K. F. Braun, V. Iancu, N. Pertaya, K. H. Rieder and S. W. Hla, *Phys. Rev. Lett.*, 2006, **96**, 246102.

23 J. R. Reimers, Y. Wang and D. S. Kosov, *J. Phys. Chem. C*, 2019, **123**, 15569-15574.

24 R. Paul, R. G. Reifenberger, T. S. Fisher and D. Y. Zemlyanov, *Chem. Mater.*, 2015, **27**, 5915-5924.

25 D. Y. Zhong, J. Franke, T. Blömker, G. Erker, L. F. Chi and H. Fuchs, *Nano Lett.*, 2009, **9**, 132-136.

26 B. W. Heinrich, L. Limot, M. V. Rastei, C. Iacovita, J. P. Bucher, D. M. Djimbi, C. Massobrio and M. Boero, *Phys. Rev. Lett.*, 2011, **107**, 216801.

27 J. Tersoff and D. R. Hamann, *Phys. Rev. Lett.*, 1983, **50**, 1998-2001.

28 D. Wortmann, S. Heinze, P. Kurz, G. Bihlmayer and S. Blügel, *Phys. Rev. Lett.*, 2001, **86**, 4132-4135.

29 S. Ouazi, S. Wedekind, G. Rodary, H. Oka, D. Sander and J. Kirschner, *Phys. Rev. Lett.*, 2012, **108**, 107206.

30 G. Rodary, S. Wedekind, D. Sander and J. Kirschner, *Jpn. J. Appl. Phys.*, 2008, **47**, 9013-9015.

31 T. Esat, R. Friedrich, F. Matthes, V. Caciuc, N. Atodiresei, S. Blügel, D. E. Bürgler, F. S. Tautz and C. M. Schneider, *Phys. Rev. B*, 2017, **95**, 094409.

32 O. Pietzsch, S. Okatov, A. Kubetzka, M. Bode, S. Heinze, A. Lichtenstein and R. Wiesendanger, *Phys. Rev. Lett.*, 2006, **96**, 237203.

33 M. J. Frisch, G. W. Trucks, H. B. Schlegel, G. E. Scuseria, M. A. Robb, J. R. Cheeseman, G. Scalmani, V. Barone, G. A. Petersson, H. Nakatsuji, X. Li, M. Caricato, A. V. Marenich, J. Bloino, B. G. Janesko, R. Gomperts, B. Mennucci, H. P. Hratchian, J. V. Ortiz, A. F. Izmaylov, J. L. Sonnenberg, Williams, F. Ding, F. Lipparini, F. Egidi, J. Goings, B. Peng, A. Petrone, T. Henderson, D. Ranasinghe, V. G. Zakrzewski, J. Gao, N. Rega, G. Zheng, W. Liang, M. Hada, M. Ehara, K. Toyota, R. Fukuda, J. Hasegawa, M. Ishida, T. Nakajima, Y. Honda, O. Kitao, H. Nakai, T. Vreven, K. Throssell, J. A. Montgomery Jr., J. E. Peralta, F. Ogliaro, M. J. Bearpark, J. J. Heyd, E. N. Brothers, K. N. Kudin, V. N. Staroverov, T. A. Keith, R. Kobayashi, J. Normand, K. Raghavachari, A. P. Rendell, J. C. Burant, S. S. Iyengar, J. Tomasi, M. Cossi, J. M. Millam, M. Klene, C. Adamo, R. Cammi, J. W. Ochterski, R. L. Martin, K. Morokuma, O. Farkas, J. B. Foresman and D. J. Fox, *Gaussian 16 Rev. A03*, Wallington, CT, 2016.

34 M. J. Frisch, G. W. Trucks, H. B. Schlegel, G. E. Scuseria, M. A. Robb, J. R. Cheeseman, G. Scalmani, V. Barone, B. Mennucci, G. A. Petersson, H. Nakatsuji, M. Caricato, X. Li, H. P. Hratchian, A. F. Izmaylov, J. Bloino, G. Zheng, J. L. Sonnenberg, M. Hada, M. Ehara, K. Toyota, R. Fukuda, J. Hasegawa, M. Ishida, T. Nakajima, Y. Honda, O. Kitao, H. Nakai, T. Vreven, J. A. Montgomery, Jr., J. E. Peralta, F. Ogliaro, M. Bearpark, J. J. Heyd, E. Brothers, K. N. Kudin, V. N. Staroverov, R. Kobayashi, J. Normand, K. Raghavachari, A. Rendell, J. C. Burant, S. S. Iyengar, J. Tomasi, M. Cossi, N. Rega, J. M. Millam, M. Klene, J. E. Knox, J. B. Cross, V. Bakken, C. Adamo, J. Jaramillo, R. Gomperts, R. E. Stratmann, O. Yazyev, A. J. Austin, R. Cammi, C. Pomelli, J. W. Ochterski, R. L. Martin, K. Morokuma, V. G. Zakrzewski, G. A. Voth, P. Salvador, J. J. Dannenberg, S. Dapprich, A. D. Daniels, Ö. Farkas, J. B. Foresman, J. V. Ortiz, J. Cioslowski, and D. J. Fox, *Gaussian 09 Rev. D.01*, Wallingford, CT, 2009.

35 R. Dennington, T. A. Keith, J. M. Millam, *GaussView Version 6*, Semichem Inc., Shawnee Mission, KS, 2016.

36 C. Lee, W. Yang and R. G. Parr, *Phys. Rev. B*, 1988, **37**, 785-789.

37 B. Miehlich, A. Savin, H. Stoll and H. Preuss, *Chem. Phys. Lett.*, 1989, **157**, 200-206.

38 A. D. Becke, *J. Chem. Phys.*, 1993, **98**, 5648-5652.

39 P. J. Stephens, F. J. Devlin, C. F. Chabalowski and M. J. Frisch, *J. Phys. Chem.*, 1994, **98**, 11623-11627.

40 A. D. Becke, *Phys. Rev. A*, 1988, **38**, 3098-3100.

41 A. D. McLean and G. S. Chandler, *J. Chem. Phys.*, 1980, **72**, 5639-5648.

42 A. J. H. Wachters, *J. Chem. Phys.*, 1970, **52**, 1033-1036.

43 P. J. Hay, *J. Chem. Phys.*, 1977, **66**, 4377-4384.

44 K. Raghavachari and G. W. Trucks, *J. Chem. Phys.*, 1989, **91**, 1062-1065.

45 K. Raghavachari, J. S. Binkley, R. Seeger and J. A. Pople, *J. Chem. Phys.*, 1980, **72**, 650-654.

46 S. Grimme, J. Antony, S. Ehrlich and H. Krieg, *J. Chem. Phys.*, 2010, **132**, 154104.

47 S. Grimme, S. Ehrlich and L. Goerigk, *J. Comput. Chem.*, 2011, **32**, 1456-1465.

48 D. G. A. Smith, L. A. Burns, K. Patkowski and C. D. Sherrill, *J. Phys. Chem. Lett.*, 2016, **7**, 2197-2203.

49 W. Humphrey, A. Dalke and K. Schulten, *Journal of Molecular Graphics*, 1996, **14**, 33-38.